

# Microlensing of the Lensed Quasar SDSS 0924+0219<sup>1</sup>

Christopher W. Morgan<sup>2</sup>

*Department of Physics, United States Naval Academy, 572C Holloway Road, Annapolis,  
MD 21402*

[cmorgan@usna.edu](mailto:cmorgan@usna.edu)

C.S. Kochanek and Nicholas D. Morgan

*Department of Astronomy, The Ohio State University, 140 West 18th Avenue, Columbus,  
OH 43201-1173*

[ckochanek@astronomy.ohio-state.edu](mailto:ckochanek@astronomy.ohio-state.edu), [nmorgan@astronomy.ohio-state.edu](mailto:nmorgan@astronomy.ohio-state.edu)

and

Emilio E. Falco

*Harvard-Smithsonian Center for Astrophysics, 60 Garden Street, Cambridge, MA, 02138*

[efalco@cfa.harvard.edu](mailto:efalco@cfa.harvard.edu)

## ABSTRACT

We analyze V, I and H band HST images and two seasons of *R*-band monitoring data for the gravitationally lensed quasar SDSS0924+0219. We clearly see that image D is a point-source image of the quasar at the center of its host galaxy. We can easily track the host galaxy of the quasar close to image D because microlensing has provided a natural coronograph that suppresses the flux of the quasar image by roughly an order of magnitude. We observe low amplitude, uncorrelated variability between the four quasar images due to microlensing, but no correlated variations that could be used to measure a time delay. Monte Carlo models of the microlensing variability provide estimates of the mean stellar mass in the lens galaxy ( $0.02M_{\odot} \lesssim \langle M \rangle \lesssim 1.0M_{\odot}$ ), the accretion disk size (the disk temperature is  $5 \times 10^4$  K at  $3.0 \times 10^{14}$  cm  $\lesssim r_s \lesssim 1.4 \times 10^{15}$  cm), and the black hole mass ( $2.0 \times 10^7 M_{\odot} \lesssim M_{BH} \eta_{0.1}^{-1/2} (L/L_E)^{1/2} \lesssim 3.3 \times 10^8 M_{\odot}$ ), all at 68% confidence. The black hole mass estimate based on microlensing is consistent with

---

<sup>2</sup>Department of Astronomy, The Ohio State University

an estimate of  $M_{BH} = (7.3 \pm 2.4) \times 10^7 M_{\odot}$  from the Mg II emission line width. If we extrapolate the best-fitting light curve models into the future, we expect the the flux of images A and B to remain relatively stable and images C and D to brighten. In particular, we estimate that image D has a roughly 12% probability of brightening by a factor of two during the next year and a 45% probability of brightening by an order of magnitude over the next decade.

*Subject headings:* cosmology: gravitational lensing - microlensing - stellar masses - quasars: individual (SDSS0924+0219) - accretion disks - dark matter

## 1. Introduction

In the standard Cold Dark Matter (CDM) galaxy model, early-type galaxies are composite objects. Their mass is dominated by an extended dark matter halo that surrounds the luminous stars of the visible galaxy; any remaining baryons are left as hot gas (White & Rees 1978). The halos grow by mergers with other halos, with a small fraction of the accreted smaller halos surviving as satellite halos (“sub-structure”) orbiting in the larger halos, but the mass fraction in these satellites is uncertain (Moore et al. 1999, Klypin et al. 1999, Gao et al. 2004, Taylor & Babul 2005 and Zentner et al. 2005). There is increasing evidence from time delay measurements (e.g. Kochanek et al. 2005) and stellar dynamical observations (e.g. locally, Romanowsky et al. 2003, and in lenses Treu & Koopmans 2002, Treu et al. 2006), that the density structure of some early-type galaxies on scales of  $1-2R_e$  is heterogeneous, but this needs to be changed from a qualitative assessment to something more quantitative. Thus the detailed balance between stars, dark matter and substructure (luminous or dark) remains a matter of debate.

One approach to addressing these problems is to monitor variability in gravitational lenses. Variability in lenses arises from two sources. Correlated variability between the

---

<sup>1</sup>Based on observations obtained with the Small and Moderate Aperture Research Telescope System (SMARTS) 1.3m, which is operated by the SMARTS Consortium, the Apache Point Observatory 3.5-meter telescope, which is owned and operated by the Astrophysical Research Consortium, the WIYN Observatory which is owned and operated by the University of Wisconsin, Indiana University, Yale University and the National Optical Astronomy Observatories (NOAO), the 6.5m Magellan Baade telescope, which is a collaboration between the observatories of the Carnegie Institution of Washington (OCIW), University of Arizona, Harvard University, University of Michigan, and Massachusetts Institute of Technology, and observations made with the NASA/ESA Hubble Space Telescope for program HST-GO-9744 of the Space Telescope Science Institute, which is operated by the Association of Universities for Research in Astronomy, Inc., under NASA contract NAS 5-26555.

images due to fluctuations in the source flux allows the measurement of the time delays  $\Delta t$  between the quasar images, which constrain the combination  $\Delta t \propto (1 - \langle \kappa \rangle)/H_0$  of the surface density near the lensed images  $\langle \kappa \rangle = \langle \Sigma \rangle / \Sigma_c$  and the Hubble constant  $H_0$  to lowest order (Kochanek 2002).<sup>2</sup> By measuring the surface density near the lensed images, we can strongly constrain the radial mass profile of the lens. Uncorrelated variability between the images is a signature of microlensing by stars in the lens galaxy. Microlensing can constrain the mass distribution because the statistics of the variations depend on the fraction of the local density in stars (Schechter & Wambsganss 2002). In addition to providing an estimate of the surface density in stars near the lensed images, microlensing can also be used to estimate the mean stellar mass in the lens and to determine the structure of quasar accretion disks. Understanding microlensing is also required to improve estimates of the substructure mass fraction in radio-quiet lenses, because most other quasar source components are affected by both substructure and microlensing. In order to use time variability in lenses to probe these astrophysical problems, we have undertaken a program to monitor roughly 25 lenses in several optical and near-IR bands. The first results of the program and a general description of our procedures are presented in Kochanek et al. (2005).

In this paper we study the four-image  $z_s = 1.52$  quasar lens SDSS 0924+0219 (Inada et al. 2003) using  $V$ ,  $I$  and  $H$ -band Hubble Space Telescope ( $HST$ ) observations and the results from two seasons of monitoring the system in the  $R$ -band. The lens galaxy is a fairly isolated  $z_l = 0.393$  (Ofek et al. 2005) early-type galaxy. The most remarkable feature of this lens is that it shows a spectacular flux ratio anomaly between the A and D images. These two images are merging at a fold caustic with a flux difference of nearly 3 magnitudes when they should have approximately equal fluxes by symmetry (Keeton et al. 2005). Keeton et al. (2006) recently measured the flux ratios in the Ly $\alpha$  line and the adjacent continuum, finding that the anomaly is weaker in the emission line but still present. This indicates that the anomaly is partly due to microlensing, since the expected size difference between the broad line region and the optical continuum emission region should matter for microlensing but be irrelevant for substructure. Unfortunately, the continued existence of the anomaly in the emission line means either that the broad line region is not large enough to eliminate the effects of microlensing or that the flux ratio anomaly in SDSS0924+0219 is due the combined effects of microlensing and substructures.

We present the HST data in §2 as well as a series of mass models for the system consisting of the observed stellar distribution embedded in a standard dark matter halo. In

---

<sup>2</sup>The dimensionless surface density  $\kappa$  is the surface density  $\Sigma$  divided by the critical surface density  $\Sigma_c \equiv c^2 D_{\text{OS}} / 4\pi G D_{\text{OL}} D_{\text{LS}}$ , where  $D_{\text{OL}}$ ,  $D_{\text{OS}}$  and  $D_{\text{LS}}$  are the angular diameter distances between the Observer, Lens and Source.

§3 we present the light curves and model them using the Monte Carlo methods of Kochanek (2004). The analysis allows us to estimate the mean stellar mass in the lens galaxy, the size of the quasar accretion disk and the mass of the black hole powering the quasar. In §3.4 we present our predictions for the expected variability of this source over the next decade. Finally, we summarize our findings in §4. All calculations in this paper assume a flat  $\Lambda$ CDM cosmology with  $h = 0.7$ ,  $\Omega_M = 0.3$  and  $\Omega_\Lambda = 0.7$ .

## 2. HST Observations and Mass Models

In this section we discuss the HST observations and our mass model fits to the astrometric and photometric measurements.

### 2.1. HST Observations

We observed the lens in the  $V$ - (F555W),  $I$ - (F814W) and  $H$ -bands (F160W) using *HST*. The  $\sim 4380$  sec  $V$ -band and the  $\sim 4600$  sec  $I$ -band images were obtained as eight dithered sub-images with the Wide Field Channel (WFC) of the Advanced Camera for Surveys (ACS) on 2003 November 18. The 5120 sec  $H$ -band image was obtained as eight dithered sub-images on 2003 November 23 using the Near-Infrared Camera and Multi-Object Spectrograph (NICMOS). The ACS data were reduced using the *pyraf multidrizzle* package, and the NICMOS data were reduced using *nicred* (see Lehár et al. 2000). We focus on the results from the new  $H$ -band image, shown in Fig. 1. The four quasar images, the central lens galaxy and an Einstein ring image of the quasar host galaxy can easily be seen.

We fit the  $H$ -band image using a photometric model consisting of four point sources and a de Vaucouleurs model for the lens galaxy. We modeled the lensed host galaxy as an exponential disk, using a singular isothermal ellipsoid (SIE) mass model for the lens galaxy. We also tried a de Vaucouleurs lens galaxy mass model, but doing so caused no significant change in the quality of the lensed host galaxy photometric fit (see Peng et al. 2006 for a discussion of systematic issues in modeling lensed host galaxies). The fits were done with *imfitfits* (see Lehár et al. 2000) using a range of bright PSF models, with the PSF producing the best overall fit being adopted for the final results. We then use the  $H$ -band fit as our reference, and we hold the astrometry and model structure fixed for the  $V$ - and  $I$ -band photometric fits. In Table 1, we present astrometric and photometric measurements for the system. Our fits to the lens astrometry and photometry are consistent with those of Keeton et al. (2006) and Eigenbrod et al. (2005).

The lens in SDSS 0924+0219 is an early-type galaxy with effective radius  $R_e = 0''.31 \pm 0''.02$ , axis ratio  $q = 0.92 \pm 0.02$ , major axis position angle  $\theta_e = -27 \pm 8^\circ$  (East of North) and colors  $V - I = 1.44 \pm 0.07$  and  $V - H = 3.60 \pm 0.05$ . Following the technique of Rusin & Kochanek (2005), we performed a Fundamental Plane (FP) analysis of the lens to determine if its observed properties fall on the track of the expected Mass-to-Light (M/L) evolution with redshift for elliptical galaxies (Rusin et al. 2003). Assuming that a nominal early-type galaxy undergoes a starburst phase at high redshift and then evolves passively thereafter, we expect elliptical galaxies to show a steady increase in M/L with decreasing redshift. If the SDSS0924+0219 lens galaxy is to lie on the present-day FP, then it requires a  $\Delta \log(M/L)$  evolution of  $-0.42 \pm 0.03$  from  $z = 0.393$  to  $z = 0$ . This is steeper than the mean value for lens galaxies around that redshift,  $\Delta \log(M/L) = -0.22 \pm 0.04$ , implying that the lens has a smaller than average M/L. Note, however, that Treu et al. (2006) find a faster evolution than Rusin et al. (2003), which would be consistent with the value we find for SDSS0924+0219.

One remarkable feature in this lens is how the stars (or a small satellite) in the lens galaxy have provided a natural coronograph at the location of image D. The quasar flux is suppressed by roughly an order of magnitude, making it very easy to see into the central regions of the host galaxy. We obtain a good fit with a host having a scale length of  $0''.11 \pm 0''.01$ , axis ratio of  $0.74 \pm 0.05$  and magnitude of  $H = 20.56 \pm 0.14$  mag. For comparison, we estimate an unmagnified magnitude of  $H = 20.40 \pm 0.20$  mag for the quasar. We also attempted a de Vaucouleurs model fit to the host galaxy, but we found that doing this resulted in a negligible change in the overall quality of fit. We are not able to discriminate between host galaxy models. We extracted the Einstein ring curve of the lens (Kochanek et al. 2001) to use as one of the constraints on the mass models.

Images A, B and C have similar  $I - H$  and  $V - I$  colors, while image D is significantly redder in  $I - H$  but of similar color in  $V - I$ . This is similar to the expected pattern for dust extinction, since an 0.5 mag difference in  $I - H$  should correspond to a 0.15 mag difference in  $V - I$  for an  $R_V = 3.1$  extinction curve shifted to the redshift of the lens. On the other hand, the Einstein ring image of the host galaxy does not show color trends near the D image, which strongly argues against dust as the origin of the color differences. Moreover the significant differences between the A/D flux ratio in Ly $\alpha$  as compared to the continuum (Keeton et al. 2006), means that microlensing must be a significant contributor to the anomalous flux ratio.

## 2.2. Macro Models and Substructure

We modeled the lens galaxy as the sum of a de Vaucouleurs model with scale length  $R_e = 0''.31$  embedded in an NFW (Navarro, Frenk & White 1996) model with a break radius  $r_c = 10''.0$ . The de Vaucouleurs and NFW models were ellipsoids constrained by the axis ratio and orientation of the lens galaxy in the  $H$ -band images, and we included an external shear to model any additional perturbations from the lens environment or along the line of sight. We constrained the mass model with the astrometry of the quasar images and the Einstein ring curve derived from the  $H$ -band images (Kochanek et al. 2001) using the GRAVLENS (Keeton 2001) software package. We required the NFW and de Vaucouleurs components to be perfectly concentric, but we permitted the combined model to move within  $0''.01$  of the measured galaxy center in order to optimize the fit. As described in detail by Kochanek (2005), it is not possible to determine the radial mass profile of the lens using these constraints, although it can be done using other constraints such as a time delay or stellar velocity dispersion measurement. Given this degeneracy, we generated a sequence of models parameterized by  $0 \leq f_{M/L} \leq 1$ , the fractional mass of the de Vaucouleurs component compared to a constant M/L model ( $f_{M/L} = 1$ ). As expected, there is no significant difference in how well models with  $0 < f_{M/L} \leq 1$  fit the constraints with the exception of pure dark matter models ( $f_{M/L} \lesssim 0.1$ ) that predict a detectable, fifth or odd quasar image near the center of the Einstein ring. The convergence, shear and  $\kappa_*/\kappa$  for the range of  $f_{M/L}$  at each image location is presented in Table 2.

Although much of the anomalous A/D flux ratio must be due to microlensing based on the smaller anomaly observed in the emission lines, we explored the extent to which the anomaly could be created by small satellites of the lens galaxy rather than by stars. For these tests we modeled the main lens as a singular isothermal ellipsoid (SIE) and then added a low-mass pseudo-Jaffe model as a perturber. We assigned the perturber Einstein radii of either  $0''.01$  or  $0''.003$  and tidal truncation radii of  $0''.1$  and  $0''.06$ , respectively. Fig. 2 shows the goodness of fit,  $\chi^2/N_{DOF}$ , as a function of the perturber’s position, where we fit both the astrometric constraints from the quasar image positions and the flux ratios from the  $H$ -band *HST* data. While the more massive satellite with an Einstein radius of  $0''.01$  has difficulty adjusting the flux ratio without violating the astrometric constraints, the lower mass satellite can do so if properly positioned. Such a satellite would have a mass of  $\sim 10^{-5}$  that of the primary lens, roughly corresponding to the mass scale of globular clusters. While the emission line flux ratios largely rule this out as a complete explanation for SDSS 0924+0219, substructure could explain the continued existence of an anomaly in the emission line flux ratios. We include this calculation as an illustration that substructure can lead to anomalies as extreme as are observed here.

### 3. Microlensing

#### 3.1. Monitoring Data and Microlensing

We have obtained somewhat more than two seasons of *R*-band monitoring data for SDSS 0924+0219. Our analysis procedures are described in detail in Kochanek et al. (2005), so we provide only a brief summary here. We measure the flux of each quasar image relative to a sample of reference stars in each frame. We keep the relative positions of the components fixed, using the *HST* astrometry for the lensed components, and derive the PSF model and quasar flux for each epoch by simultaneously fitting the lens and the reference stars. The PSF is modeled by 3 nested, elliptical Gaussian components. The galaxy is included in the model at a constant flux which we determine by fitting all the data as a function of the galaxy flux and then adopting the galaxy flux that produces the best fit to the complete data set. We confirm that the lens galaxy flux is approximately constant at each epoch by examination of the residual galaxy flux after subtraction of the best-fit models, and we find no evidence for variability during our three seasons of monitoring.

Most of our observations were obtained at the queue-scheduled SMARTS 1.3m using the ANDICAM optical/infrared camera (DePoy et al. 2003).<sup>3</sup> Additional observations were obtained at the Wisconsin-Yale-Indiana (WIYN) observatory using the WIYN Tip-Tilt Module (WTTM)<sup>4</sup>, the 2.4m telescope at the MDM Observatory using the MDM Eight-K<sup>5</sup>, Echelle and RETROCAM<sup>6</sup> (Morgan et al. 2005) imagers, the 3.5m APO telescope using Spicam and the 6.5m Magellan Baade telescope using IMACS (Bigelow et al. 1999). Images taken under seeing conditions worse than 1''.5 were discarded. We also added the photometry from Inada et al. (2003) to extend our baseline to nearly four years for the microlensing calculations. The *R*-band light curves are displayed in Fig. 3, and the data are presented in Table 3.

In Fig. 3, we also show the *HST* *V*-band photometry scaled to the best-fit *R*-band monitoring magnitude of Image A on the observation date. In the *HST* data, image D is  $\sim 1$  mag fainter relative to image A than our estimate on nearly the same date. After considerable experimentation, we concluded that our flux for image D may be contaminated by image A, although we found no correlation between the A/D flux ratio and the seeing.

---

<sup>3</sup><http://www.astronomy.ohio-state.edu/ANDICAM/>

<sup>4</sup>[http://www.wiyn.org/wttm/WTTM\\_manual.html](http://www.wiyn.org/wttm/WTTM_manual.html)

<sup>5</sup><http://www.astro.columbia.edu/arlin/MDM8K/>

<sup>6</sup><http://www.astronomy.ohio-state.edu/MDM/RETROCAM>

Nonetheless, we include estimates of seeing at each observation epoch in Table 3. In the calculations that follow we will use both our image D light curve as observed and an image D light curve shifted 1 mag fainter to agree with the *HST* flux ratio. The shift had little effect on our results in § 3.2–3.4.

In our mass models, the longest expected delay for the system is  $\sim 10$  days for  $H_0 = 72 \text{ km s}^{-1} \text{ Mpc}^{-1}$ . We see little evidence for correlated variability between the images on these time scales, so we cannot measure the time delays. For the present study, it seems safe to simply ignore the time delays.

### 3.2. Microlensing Models

For each of our macro models, parameterized by  $f_{M/L}$ , we generated 8 random realizations of the expected microlensing magnification patterns for each image. We used patterns with an outer dimension of  $20R_e$  where  $R_e = 5.7 \times 10^{16} \langle M/M_\odot \rangle^{1/2} \text{ cm}$  is the Einstein radius for the average mass star. The map dimensions were  $8192^2$ , so we can model source sizes down to  $3 \times 10^{-3}R_e$ . The stars used to create the patterns were drawn from a Salpeter IMF with a dynamic range in mass of a factor of one hundred. We modeled the accretion disk of the quasar as a standard, face-on thin disk model (Shakura & Sunyaev 1973) with a scale length of  $r_s = \hat{r}_s \langle M/M_\odot \rangle^{1/2}$  where the microlensing behavior is determined by the source size scaled by the mean mass of the microlenses,  $\hat{r}_s$ . We have chosen to use a thin disk model because it provides a context for interpreting the results, but Mortonson et al. (2005) have shown that  $r_s$  can simply be interpreted as the typical half-light radius for any choice of emission profile. We do, however, neglect the central hole in the disk emissivity to avoid the introduction of an additional parameter. We fit the light curves using the Monte Carlo method of Kochanek (2004). In this method, large numbers of trial light curves are randomly generated and fitted to the observed light curves. Bayesian statistical methods are used to combine the resulting distributions of  $\chi^2$  values for the fits to the light curves to obtain probability distributions for the model parameters.

We are interested in models where microlensing is responsible for any deviations of the image flux ratios from the lens model, so we assumed that the flux ratios of the macro model were correct up to a systematic uncertainty of 0.05 mag for images A–C and 0.1 mag for image D. We also allowed for an 0.02 mag systematic uncertainty in the photometry of images A–C and an 0.1 mag systematic uncertainty in the photometry of image D. These errors were added because the point-to-point scatter in the light curves is somewhat broader than the formal uncertainties in the photometry. With these assumptions, we have no difficulty finding light curves that fit the data well, with  $\chi^2/N_{DOF} \approx 1.0$ . We generated  $10^5$  trial light curves

for each source size, magnification pattern and mass model. Several example light curves which provide good fits to the data are shown in Fig. 4. For each reasonable fit to the light curves, defined by  $\chi^2/N_{DOF} \leq 2.3$ , we also generated an extrapolated light curve extending for an additional ten years beyond the last data point of the third season (2005 December 14; HJD 2453719). We also repeated all the calculations shifting the image D light curve 1 mag fainter to match the HST observations, finding few changes in the results.

In order to convert the results from Einstein radius units, where all physical scales depend on the mean mass of the microlenses  $\langle M/M_\odot \rangle$ , we must assume either a probability distribution for the actual velocities or a prior for the mean stellar mass. Our velocity model includes the 176 km s<sup>-1</sup> projected velocity of the CMB dipole onto the plane of the lens, a probability distribution for the one-dimensional peculiar velocity dispersion of galaxies at  $z_l$  with rms value of 164 km s<sup>-1</sup> and a one-dimensional stellar velocity dispersion in the lens galaxy of 219 km s<sup>-1</sup> based on the Einstein radius of the lens and an isothermal lens model. As discussed in detail by Kochanek (2004), the lens galaxy peculiar velocity dispersion and stellar velocity dispersion estimates are dependent upon the selected cosmology. We have chosen the standard flat concordance cosmology ( $\Omega_M = 0.3$  and  $\Omega_\Lambda = 0.7$ ) for our estimates. We also consider the consequences of using a limited range for the mean stellar mass of  $0.1 \leq \langle M/M_\odot \rangle < 1.0$ .

Figures 5 and 6 show the results for the system motions and the lens galaxy stellar mass estimate. The large flux ratio anomalies combined with the limited amount of observed variability means that the effective velocity in the system must be relatively low. We find that  $280 \text{ km s}^{-1} \lesssim \hat{v}_e \lesssim 749 \text{ km s}^{-1}$  (68% confidence), and this changes little if we adjust the D image light curve to be 1 mag fainter. If we compare the effective velocity distribution to our model for the possible distribution of physical velocities (Fig. 5), we can estimate the mean microlens mass since the two velocities are related by  $\hat{v}_e = v_e/\langle M/M_\odot \rangle^{1/2}$ . The broad range permitted for  $\hat{v}_e$  translates into a broad range for the stellar mass estimates, with  $0.02 M_\odot \lesssim \langle M \rangle \lesssim 1.0 M_\odot$  (68% confidence). The low mass solutions correspond to large sources with high effective velocities and the high mass solutions correspond to small sources with low effective velocities.

We were somewhat surprised to find that the present data do not distinguish between the lens models at all because we had based our expectations on the (Schechter & Wambsganss 2002) picture in which models with low  $\kappa_*/\kappa$  dominate the probability of finding a faint saddle point image like D. We found instead that the probability distribution for  $f_{M/L}$  is basically flat. This result is little affected by imposing the prior on the permitted mass range of the microlenses or by adjusting the image D light curve to be 1 mag fainter. In comparison, the microlensing models for SDSS 0924+0219 by Keeton et al. (2006) strongly favored models

with low  $\kappa_*/\kappa$ . We believe the differences between the results are due to our use of finite-sized sources, which significantly enhance the probability of large demagnifications relative to large magnifications because the high magnification regions (caustics) are more affected by finite source sizes. Another source of differences is that we are analyzing a more strongly constrained problem by requiring that the models fit the observed light curves rather than simply fit the instantaneous flux ratios.

### 3.3. Quasar Structure

One objective of our monitoring program is to study the structure of quasar accretion disks. We start by estimating the black hole mass using the  $M_{BH}$ , Mg II line width, luminosity relations of McLure & Jarvis (2002) and Kollmeier et al. (2005). We measured the Mg II(2800Å) line width in spectra obtained by Ofek et al. (2005) following the procedures detailed in Kollmeier et al. (2005), and we estimated the magnification-corrected continuum luminosity at 3000Å,  $L_\lambda(3000\text{\AA})$ , using a power law fit to our HST data. For the McLure & Jarvis (2002) calibration we find a black hole mass of  $M_{BH} = (6.3 \pm 1.5) \times 10^7 M_\odot$ , and for the (Kollmeier et al. 2005) calibration we find  $M_{BH} = (7.3 \pm 2.4) \times 10^7 M_\odot$ . We adopt the estimate based on the Kollmeier et al. (2005) calibration. Similarly, we estimate that the magnification-corrected bolometric luminosity of the quasar is  $L_{bol} = (2.7 \pm 1.3) \times 10^{45} \text{ erg s}^{-1}$  where we follow Kaspi et al. (2000) in assuming that  $L_{bol} \simeq 9 \times \lambda L_\lambda(5100\text{\AA})$ . This bolometric luminosity corresponds to an accretion rate  $\dot{M} = (0.48 \pm 0.24) \eta_{0.1}^{-1} M_\odot \text{ yr}^{-1}$ , where  $\eta = 0.1 \eta_{0.1}$  is the radiative efficiency of the accretion. Fig. 7 summarizes these “classical” constraints on the quasar.

The new constraint we obtain from the microlensing observations is on the size  $r_s$  of the quasar, which we can also estimate using our accretion disk model and the observed flux. A standard thin disk model (Shakura & Sunyaev 1973) radiates as a black body with a temperature profile of  $T = T_s(R/r_s)^{-3/4}$ , and the scale length we measure should correspond to the point in the disk where the temperature corresponds to the rest-frame wavelength of the filter band pass. For our  $R$ -band data (2770Å in the quasar rest frame), our scale length corresponds to the point where  $T_s(r_s) \simeq 5.2 \times 10^4$  K. If the viscous energy release is radiated locally and we are well removed from the Schwarzschild radius, then the disk temperature and scale length are related to the black hole mass  $M_{BH}$  and accretion rate  $\dot{M}$  by

$$\sigma T_s^4 = 3GM_{BH}\dot{M}/8\pi r_s^3 \quad (1)$$

(Shakura & Sunyaev 1973), so a measurement of  $r_s$  constrains the product  $M_{BH}\dot{M}$ . One means of estimating  $r_s$  is to simply compute what it must be to produce the observed  $R$ -

band flux. Again assuming a standard, face-on thin disk, the emission profile is

$$I(R) \propto [\exp((R/r_s)^{3/4}) - 1]^{-1} \quad (2)$$

(Shakura & Sunyaev 1973). Assuming that the disk radiates locally as a blackbody, we integrate this emission profile over the physical extent of the disk to estimate its specific luminosity  $L_{\nu,em}$  in the rest frame. Incorporating the system’s geometry and correcting for redshift effects, we convert  $L_{\nu,em}$  to  $F_{\lambda,obs}$ , the specific flux in the observed frame. We then solve  $F_{\lambda,obs}$  for  $r_s$  to yield

$$r_{s_{\lambda,obs}} = 2.83 \times 10^{15} \frac{1}{\sqrt{\cos i}} \left( \frac{D_{OS}}{r_H} \right) \left( \frac{\lambda_{obs}}{\mu\text{m}} \right)^{3/2} 10^{-0.2(M_{\lambda_{obs}} - 19)} h^{-1} \text{ cm}, \quad (3)$$

where  $M_{\lambda,obs}$  is the observed magnitude,  $D_{OS}/r_H$  is the angular diameter distance to the quasar in units of the Hubble radius and  $i$  is the disk inclination angle, assumed to have an average value  $\langle i \rangle = 60^\circ$ . For SDSS 0924+0219, we find an unmagnified *HST I*-band magnitude  $I = 21.24 \pm 0.25$  mag, yielding the scale radius at the redshifted center of the *HST I*-band,  $r_{s_{I,obs}} = 6.3 \pm 1.6 \times 10^{14}$  cm. Assuming the  $T^{-4/3}$  scaling of thin disk theory, we estimate an *R*-band disk size of  $r_{s_{R,obs}} = 5.0 \pm 1.3 \times 10^{14}$  cm. We show the resulting constraint on  $M_{BH}\dot{M}$  in Fig. 7.

Microlensing tests this theoretical calculation because the amplitude of the microlensing variability is controlled by the projected area of the source that smooths the magnification patterns. Fig. 8 shows our estimate of the scaled *R*-band source size  $\hat{r}_s$ , which is related to the physical source size by  $r_s = \hat{r}_s \langle M/M_\odot \rangle^{1/2}$ . The source must be quite compact relative to the Einstein radius of the typical microlens, with an exact bound that is presently difficult to determine because of the limited level of observed variability. We face two technical problems in extending Fig. 8 to smaller source sizes. The first problem is that our analysis code is presently limited to  $8192^2$  magnification patterns, so when using an outer dimension large enough to produce a reasonable statistical representation of the magnification patterns it is difficult to resolve such small scales. The second problem is that even if we could resolve the smallest scales, we would find that the probability distribution flattens and becomes constant at small scale lengths. This occurs because the differences between small smoothing lengths are detectable only during caustic crossings – if our light curves do not extend to within a source size of a caustic, there is little effect from using a still smaller source size. Complete convergence at small scales will require a light curve with caustic crossings.

Despite these problems, we can estimate the physical source size of the accretion disk reasonably well because there is a fairly strong degeneracy between the scaled source size  $\hat{r}_s$ , the scaled velocity  $\hat{v}_e$  and the microlens mass scale  $\langle M/M_\odot \rangle$  in the sense that more compact sources require smaller scaled velocities which implies a larger microlens mass scale for the

conversion to the physical source size (see Kochanek 2004). Fig. 9 shows the estimates of the physical size  $r_s$  both with and without the prior on the microlens masses. Reassuringly, the results depend only weakly on the prior. Nonetheless, we will adopt the results with the mass prior:  $3.0 \times 10^{14} \text{ cm} \lesssim r_s \lesssim 1.4 \times 10^{15} \text{ cm}$  at 68% confidence. This is consistent with our earlier estimate from the continuum flux but is a weaker constraint on  $M_{BH} \dot{M}$ , as shown in Fig. 7.

### 3.4. Expectations for the Future Behavior of SDSS0924+0219

For each light curve which passed a threshold of  $\chi^2/N_{DOF} \leq 2.3$ , we generated a light curve for a period of ten years beyond our most recent observation. For each image, we then tracked the maximum change in the brightness in both the positive and negative directions on 1, 3 and 10 year time scales. The normalized, cumulative distributions of these maximum changes are shown in Fig. 10. One of the more obvious predictions of Fig. 10 is that images A and B are likely to remain constant while images C and D are likely to become brighter. One of the original motivations of this study was to estimate the time scale on which the flux ratio anomaly would vanish as D moved out of a low-magnification region and became brighter. Here we find an approximately 12% chance that it will brighten by at least a factor of 2 in the course of the next year and a roughly 45% chance that it will brighten by more than an order of magnitude over the next decade. For the separate calculation in which we lowered the flux of all points on the image D light curve by +1 magnitude, we predict a 9% probability of image D brightening by a factor of two during the next year, and a 53% chance that image D will brighten by a factor of ten during the next ten years.

Our expectation that D brightening would be the means of solving the anomaly was based on the preconception that D was a de-magnified saddle point in a model with a small ratio between the stellar and total surface densities  $\kappa_*/\kappa$ . Schechter & Wambsganss (2002) demonstrated that in this regime there is an appreciable probability of strongly de-magnifying saddle point images like D. Our results confirm this finding.

## 4. Conclusions

During the course of our monitoring campaign we have observed uncorrelated variability in the four images of SDSS 0924+0219, evidence that microlensing is occurring in this system. Furthermore, our models demonstrate that microlensing is a viable explanation for the system’s anomalous flux ratios. This study does not rule out the alternative hypothesis

that dark matter substructure contributes to the anomaly, but it does firmly establish the presence of microlensing variability and the ability of microlensing to explain the anomaly. As we continue to monitor SDSS 0924+0219, we expect to eventually measure the time delay, thereby restricting the range of permissible halo models, and to steadily reduce the uncertainties in the estimated mean stellar mass, accretion disk structure and black hole mass. At some point over the next few years, we should also see dramatic changes in the fluxes of the merging images.

We can also begin to compare microlensing estimates of the structure of quasar accretion disks. In our original study (Kochanek 2004), we modeled the significantly more luminous, but very similar redshift, quasar Q2237+0305 ( $M_V = -25.8 \pm 0.5$  versus  $M_V = -21.7 \pm 0.7$  after correcting for magnification). As we would expect from accretion disk theory, the microlensing analyses indicate that the more luminous quasar has a significantly larger scale ( $r_s \simeq 4.1 \times 10^{15}$  cm versus  $r_s \simeq 6.9 \times 10^{14}$  cm) and black hole mass ( $M_{BH} \simeq 1.1 \times 10^9 M_\odot$  versus  $1.3 \times 10^8 M_\odot$ ). The next step is to combine the microlensing analyses of many lenses to explore these correlations in detail and to use the wavelength dependence of the microlensing variability to study the structure of individual disks. This next step should be possible very shortly.

We thank E. Turner for providing data from APO and P. Schechter and W. Barkhouse for the data from Magellan. We thank E. Agol for discovering an error in the original manuscript. We thank C. Onken, B. Peterson and R. Pogge for discussions about quasar structure and black hole mass estimation from emission line widths. This research made extensive use of a Beowulf computer cluster obtained through the Cluster Ohio program of the Ohio Supercomputer Center. Support for program HST-GO-9744 was provided by NASA through a grant from the Space Telescope Science Institute, which is operated by the Association of Universities for Research in Astronomy, Inc., under NASA contract NAS-5-26666.

*Facilities:* HST (NICMOS, ACS), Hiltner (EIGHTK, Echelle, RETROCAM), ARC (Spicam), WIYN (WTTM), CTIO:2MASS (ANDICAM)

## REFERENCES

Bigelow, B.C., Dressler, A.M., Schechtman, S.A. & Epps, H.W. 1999, SPIE, 3355, 12  
Dalal, N. & Kochanek, C.S. 2002, ApJ, 572, 25  
DePoy, D.L., Atwood, B., Belville, S.R., Brewer, D.F., Byard, P.L., Gould, A., Mason, J.A.,

O'Brien, T.P., Pappalardo, D.P., Pogge, R.W., Steinbrecher, D.P., & Tiega, E.J., 2003, SPIE, 4841, 827

Eigenbrod, A., Courbin, F., Dye, S., Meylan, G., Sluse, D., Saha, P., Vuissoz, C. & Magain, P. 2006, A&A, 451, 747

Gao, L., White, S.D.M., Jenkins, A., Stoehr, F. & Springel, V. 2004, MNRAS, 355, 819

Inada, N., et al., 2003, AJ, 126, 666

Kaspi, S. Smith, P.S., Netzer, H., Maoz, D., Jannuzi, B.T. & Giveon, U. 2000, ApJ, 553, 631

Keeton, C.R. 2001, preprint, [astro-ph/0102340]

Keeton, C.R., Gaudi, B.S., & Petters, A.O. 2005, ApJ, 635, 35

Keeton, C. R., Burles, S., Schechter, P.L. & Wambsganss, J. 2006, ApJ, 639, 1

Klypin, A., Kravtsov, A.V., Valenzuela, O. & Prada, F. 1999, ApJ, 522, 8

Kochanek, C.S., 2002, ApJ, 578, 25

Kochanek, C.S. 2004, ApJ, 605, 58

Kochanek, C.S., 2005, Strong Gravitational Lensing, Part 2 of Gravitational Lensing: Strong, Weak & Micro, Proceedings of the 33rd Saas-Fe Advanced Course, G. Meylan, P. Jetzer & P. North, eds. (Springer Verlag: Berlin) [astro-ph/0407232]

Kochanek, C.S., Keeton, C.R. & McLeod, B.A. 2001 ApJ, 547, 50

Kochanek, C.S., Morgan, N.D., Falco, E.E. McLeod, B.A., Winn, J. Demibicky, J. & Ketzeback, B. 2006, ApJ, 640, 47

Kollmeier, J.A. et al. 2006, ApJ, 648, 128

Lehár, J., Falco, E.E, Kochanek, C.S., McLeod, B.A., Impey, C.D., Rix, H.-W., Keeton, C.R. & Peng, C.Y. 2000, ApJ, 536, 584

McLure, R.J. & Jarvis, M.J. 2002, MNRAS, 337, 109

Moore, B., Ghigna, S., Governato, F., Lake, G., Quinn, T., Stadel, J. & Tozzi, P. 1999, ApJ, 524, L19

Morgan, C.W., Byard, P.L., DePoy, D.L., Derwent, M., Kochanek, C.S., Marshall, J.L., O'Brien, T.P. & Pogge, R.P. 2005, AJ, 129, 2504

Mortenson, M.J., Schechter, P.L. & Wambsganss, J. 2005, ApJ, 628, 594

Navarro, J.F., Frenk, C.S. & White S.D.M. 1996, ApJ, 462, 563

Ofek, E.O., Maoz, D., Rix, H.-W., Kochanek, C.S., & Falco, E.E. 2005, ApJ, submitted, [astro-ph/0510465]

Peng, C.Y., Impey, C.D., Rix, H.-W., Kochanek, C.S., Keeton, C.R., Falco, E.E., Lehár, J. & McLeod, B.A. 2006, ApJ, 649, 616

Peterson, B.M., et al. 2004, ApJ, 613, 682

Romanowski, A.J., Douglas, N.G., Arnaboldi, W., Kuijken, K., Merrifield, M.R., Napolitano, N.R., Capaccioli, M. & Freeman, K.C. 2003, Science, 301, 1696

Rusin, D., Kochanek, C.S., Falco, E.E., Keeton, C.R., McLeod, B.A., Impey, C.D., Lehár, J., Muñoz, J.A., Peng, C.Y., Rix, H.-W. 2003, ApJ, 587, 143

Rusin, D. & Kochanek, C.S. 2005, ApJ, 623, 666

Schechter, P. L., & Wambsganss, J. 2002, ApJ, 580, 685

Shakura, N.I. & Sunyaev, R.A., A&A, 24, 337

Taylor, J.E. & Babul, A. 2005, MNRAS, in press

Treu, T. & Koopmans, L.V.E. 2002, MNRAS, 337, 6

Treu, T., Koopmans, L.V.E., Bolton, A.S., Burles, S., & Moustakas, L.A. 2006, ApJ, 640, 662

White, S.D.M & Rees M.J. 1978, MNRAS, 183, 341

Zentner, A.R., Berlind, A.A., Bullock, J.S., Kravtsov, A.V. & Wechsler, R.S. 2005, ApJ, 625, 505

Table 1. HST Astrometry and Photometry of SDSS0924+0219

Component	Astrometry		Photometry		
	$\Delta\text{RA}$	$\Delta\text{Dec}$	H=F160W	I=F814W	V=F555W
A	$\equiv 0$	$\equiv 0$	$17.96 \pm 0.02$	$18.77 \pm 0.05$	$19.61 \pm 0.01$
B	$+0''.061 \pm 0''.003$	$-1''.805 \pm 0''.003$	$18.87 \pm 0.03$	$19.64 \pm 0.07$	$20.36 \pm 0.05$
C	$-0''.968 \pm 0''.003$	$-0''.676 \pm 0''.005$	$19.22 \pm 0.02$	$20.22 \pm 0.09$	$20.74 \pm 0.09$
D	$+0''.536 \pm 0''.003$	$-0''.427 \pm 0''.003$	$20.64 \pm 0.06$	$22.00 \pm 0.22$	$22.94 \pm 0.13$
G	$-0''.183 \pm 0''.004$	$-0''.858 \pm 0''.004$	$17.23 \pm 0.04$	$19.39 \pm 0.06$	$20.83 \pm 0.03$

Table 2. Macroscopic Lens Mass Models

$f_{M/L}$	Convergence $\kappa$				Shear $\gamma$				$\kappa_*/\kappa$			
	A	B	C	D	A	B	C	D	A	B	C	D
0.1	0.74	0.71	0.77	0.75	0.24	0.21	0.29	0.28	0.020	0.018	0.024	0.021
0.2	0.67	0.65	0.70	0.67	0.30	0.26	0.37	0.36	0.042	0.038	0.050	0.044
0.3	0.61	0.59	0.64	0.61	0.35	0.30	0.44	0.43	0.061	0.055	0.072	0.062
0.4	0.53	0.51	0.56	0.53	0.42	0.36	0.53	0.52	0.11	0.10	0.13	0.11
0.5	0.47	0.45	0.49	0.46	0.48	0.41	0.61	0.60	0.15	0.14	0.17	0.15
0.6	0.40	0.38	0.44	0.41	0.54	0.45	0.69	0.67	0.19	0.18	0.23	0.20
0.7	0.31	0.29	0.35	0.31	0.62	0.51	0.80	0.77	0.34	0.32	0.38	0.34
0.8	0.25	0.23	0.29	0.26	0.67	0.55	0.88	0.84	0.45	0.42	0.50	0.46
0.9	0.17	0.16	0.22	0.18	0.73	0.61	0.96	0.92	0.72	0.70	0.77	0.73
1.0	0.13	0.12	0.17	0.13	0.77	0.64	1.02	0.98	1.00	1.00	1.00	1.00

Note. — Convergence  $\kappa$ , shear  $\gamma$  and the fraction of the total surface density composed of stars  $\kappa_*/\kappa$  at each image location for the series of macroscopic mass models.

Table 3. SDSS0924+0219 Light curves

HJD	$\chi^2/N_{dof}$	Seeing	QSO A	QSO B	QSO C	QSO D	$\langle \text{Stars} \rangle$	Source
2957.814	0.70	1''22	2.812 $\pm$ 0.028	3.515 $\pm$ 0.033	3.883 $\pm$ 0.054	5.041 $\pm$ 0.217	-0.032 $\pm$ 0.003	SMARTS
2964.789	0.65	1''42	2.864 $\pm$ 0.024	3.516 $\pm$ 0.024	3.895 $\pm$ 0.042	4.840 $\pm$ 0.144	0.004 $\pm$ 0.003	SMARTS
2976.775	0.64	1''31	2.800 $\pm$ 0.020	3.464 $\pm$ 0.022	3.892 $\pm$ 0.039	5.006 $\pm$ 0.149	-0.001 $\pm$ 0.003	SMARTS
2984.721	0.56	1''20	2.811 $\pm$ 0.036	3.453 $\pm$ 0.040	3.852 $\pm$ 0.068	4.632 $\pm$ 0.189	-0.037 $\pm$ 0.003	SMARTS
2991.791	0.79	1''08	2.766 $\pm$ 0.016	3.531 $\pm$ 0.019	3.991 $\pm$ 0.033	5.138 $\pm$ 0.128	0.012 $\pm$ 0.003	SMARTS
2995.932	1.82	1''20	2.785 $\pm$ 0.012	3.507 $\pm$ 0.013	3.928 $\pm$ 0.022	5.147 $\pm$ 0.105	0.084 $\pm$ 0.002	MDM-EIGHTK
2998.787	1.31	0''94	2.804 $\pm$ 0.014	3.541 $\pm$ 0.017	4.047 $\pm$ 0.029	5.258 $\pm$ 0.120	0.027 $\pm$ 0.003	SMARTS
3022.797	1.82	1''09	2.882 $\pm$ 0.019	3.417 $\pm$ 0.018	4.161 $\pm$ 0.037	4.937 $\pm$ 0.116	0.015 $\pm$ 0.003	SMARTS
3029.751	2.13	0''90	2.865 $\pm$ 0.014	3.386 $\pm$ 0.015	4.187 $\pm$ 0.029	5.092 $\pm$ 0.092	0.021 $\pm$ 0.003	SMARTS
3036.673	0.70	0''99	2.780 $\pm$ 0.016	3.441 $\pm$ 0.019	4.216 $\pm$ 0.042	5.209 $\pm$ 0.144	0.004 $\pm$ 0.003	SMARTS
3047.794	0.94	1''31	2.749 $\pm$ 0.024	3.408 $\pm$ 0.024	4.331 $\pm$ 0.063	5.033 $\pm$ 0.193	-0.013 $\pm$ 0.003	SMARTS
3055.689	0.68	1''13	2.819 $\pm$ 0.009	3.555 $\pm$ 0.012	4.206 $\pm$ 0.020	5.353 $\pm$ 0.071	-0.025 $\pm$ 0.002	MAGELLAN
3056.744	0.80	1''11	2.757 $\pm$ 0.016	3.428 $\pm$ 0.017	4.201 $\pm$ 0.036	5.152 $\pm$ 0.133	0.016 $\pm$ 0.003	SMARTS
3064.680	1.30	1''08	2.836 $\pm$ 0.018	3.381 $\pm$ 0.018	4.187 $\pm$ 0.039	4.948 $\pm$ 0.119	0.010 $\pm$ 0.003	SMARTS
3065.805	0.61	1''28	2.832 $\pm$ 0.018	3.389 $\pm$ 0.017	4.179 $\pm$ 0.039	4.560 $\pm$ 0.091	0.080 $\pm$ 0.002	MDM-ECHELLE
3071.649	0.53	1''08	2.800 $\pm$ 0.033	3.423 $\pm$ 0.039	4.269 $\pm$ 0.092	4.782 $\pm$ 0.206	-0.044 $\pm$ 0.003	SMARTS
3075.774	4.24	1''07	2.828 $\pm$ 0.012	3.491 $\pm$ 0.013	4.005 $\pm$ 0.022	5.046 $\pm$ 0.091	0.053 $\pm$ 0.002	MDM-EIGHTK
3078.586	0.57	1''14	2.791 $\pm$ 0.019	3.446 $\pm$ 0.020	4.234 $\pm$ 0.045	4.888 $\pm$ 0.128	0.007 $\pm$ 0.003	SMARTS
3080.834	0.56	1''31	2.797 $\pm$ 0.017	3.419 $\pm$ 0.016	4.268 $\pm$ 0.041	4.742 $\pm$ 0.098	-0.002 $\pm$ 0.003	APO
3087.648	1.49	0''86	2.770 $\pm$ 0.007	3.408 $\pm$ 0.008	4.294 $\pm$ 0.012	5.384 $\pm$ 0.043	0.188 $\pm$ 0.003	WIYN-WTTM
3089.599	1.11	1''04	2.781 $\pm$ 0.016	3.409 $\pm$ 0.017	4.198 $\pm$ 0.036	5.150 $\pm$ 0.126	0.011 $\pm$ 0.003	SMARTS
3090.666	0.79	1''50	2.833 $\pm$ 0.018	3.336 $\pm$ 0.013	4.450 $\pm$ 0.041	4.372 $\pm$ 0.066	0.168 $\pm$ 0.003	WIYN-WTTM
3101.623	0.60	1''20	2.732 $\pm$ 0.033	3.417 $\pm$ 0.037	4.420 $\pm$ 0.103	4.567 $\pm$ 0.179	-0.049 $\pm$ 0.003	SMARTS
3108.511	2.18	1''02	2.710 $\pm$ 0.016	3.361 $\pm$ 0.018	4.213 $\pm$ 0.039	5.063 $\pm$ 0.129	0.009 $\pm$ 0.003	SMARTS
3115.562	1.11	1''19	2.697 $\pm$ 0.019	3.398 $\pm$ 0.020	4.273 $\pm$ 0.049	4.889 $\pm$ 0.140	0.003 $\pm$ 0.003	SMARTS
3127.473	0.88	0''92	2.702 $\pm$ 0.020	3.364 $\pm$ 0.025	4.249 $\pm$ 0.058	4.735 $\pm$ 0.133	-0.022 $\pm$ 0.003	SMARTS
3134.453	0.79	0''91	2.631 $\pm$ 0.021	3.467 $\pm$ 0.031	4.442 $\pm$ 0.080	4.861 $\pm$ 0.167	-0.035 $\pm$ 0.003	SMARTS
3141.510	0.82	1''10	2.653 $\pm$ 0.021	3.467 $\pm$ 0.025	4.348 $\pm$ 0.060	4.638 $\pm$ 0.131	-0.018 $\pm$ 0.003	SMARTS
3159.468	0.69	1''07	2.596 $\pm$ 0.024	3.484 $\pm$ 0.035	4.382 $\pm$ 0.087	5.053 $\pm$ 0.238	-0.044 $\pm$ 0.003	SMARTS
3169.462	0.79	1''28	2.635 $\pm$ 0.020	3.582 $\pm$ 0.025	4.269 $\pm$ 0.057	5.135 $\pm$ 0.200	-0.012 $\pm$ 0.003	SMARTS
3324.813	0.42	1''44	2.675 $\pm$ 0.030	3.882 $\pm$ 0.047	4.450 $\pm$ 0.099	5.528 $\pm$ 0.404	-0.032 $\pm$ 0.003	SMARTS
3327.800	0.74	1''46	2.740 $\pm$ 0.027	3.960 $\pm$ 0.042	4.429 $\pm$ 0.083	5.217 $\pm$ 0.265	-0.016 $\pm$ 0.003	SMARTS
3330.766	0.74	1''45	2.776 $\pm$ 0.037	4.050 $\pm$ 0.067	4.466 $\pm$ 0.118	5.129 $\pm$ 0.317	-0.038 $\pm$ 0.003	SMARTS
3344.723	0.89	1''43	2.767 $\pm$ 0.026	3.923 $\pm$ 0.039	4.628 $\pm$ 0.096	5.754 $\pm$ 0.399	-0.018 $\pm$ 0.003	SMARTS
3349.758	0.56	1''49	2.703 $\pm$ 0.032	3.953 $\pm$ 0.048	4.971 $\pm$ 0.157	5.441 $\pm$ 0.384	-0.020 $\pm$ 0.003	SMARTS
3357.714	1.08	1''26	2.765 $\pm$ 0.021	3.869 $\pm$ 0.029	4.586 $\pm$ 0.069	5.674 $\pm$ 0.297	0.003 $\pm$ 0.003	SMARTS
3360.767	1.57	1''14	2.799 $\pm$ 0.020	3.841 $\pm$ 0.026	4.544 $\pm$ 0.056	5.306 $\pm$ 0.192	0.007 $\pm$ 0.003	SMARTS
3376.734	1.05	1''15	2.780 $\pm$ 0.019	3.926 $\pm$ 0.029	4.533 $\pm$ 0.058	5.379 $\pm$ 0.202	0.006 $\pm$ 0.003	SMARTS
3382.701	0.61	1''17	2.772 $\pm$ 0.022	4.012 $\pm$ 0.039	4.674 $\pm$ 0.082	5.468 $\pm$ 0.255	-0.017 $\pm$ 0.003	SMARTS
3394.741	0.61	0''98	2.779 $\pm$ 0.030	3.919 $\pm$ 0.064	4.908 $\pm$ 0.168	5.616 $\pm$ 0.426	-0.044 $\pm$ 0.003	SMARTS
3403.751	1.00	0''98	2.801 $\pm$ 0.018	3.934 $\pm$ 0.028	4.733 $\pm$ 0.062	5.107 $\pm$ 0.141	0.003 $\pm$ 0.003	SMARTS
3410.781	0.99	1''13	2.767 $\pm$ 0.019	3.905 $\pm$ 0.028	4.681 $\pm$ 0.066	5.257 $\pm$ 0.183	-0.001 $\pm$ 0.003	SMARTS
3427.737	0.55	1''32	2.705 $\pm$ 0.041	4.025 $\pm$ 0.085	5.074 $\pm$ 0.247	5.181 $\pm$ 0.399	-0.031 $\pm$ 0.003	SMARTS
3435.698	1.29	0''99	2.793 $\pm$ 0.019	3.872 $\pm$ 0.029	4.666 $\pm$ 0.063	5.155 $\pm$ 0.158	-0.013 $\pm$ 0.003	SMARTS
3443.698	1.45	1''29	2.783 $\pm$ 0.024	3.900 $\pm$ 0.033	4.692 $\pm$ 0.080	4.858 $\pm$ 0.161	-0.006 $\pm$ 0.003	SMARTS

Table 3—Continued

HJD	$\chi^2/N_{dof}$	Seeing	QSO A	QSO B	QSO C	QSO D	$\langle \text{Stars} \rangle$	Source
3450.662	0.66	1''20	2.701 $\pm$ 0.038	3.763 $\pm$ 0.066	5.006 $\pm$ 0.224	6.019 $\pm$ 0.807	-0.031 $\pm$ 0.003	SMARTS
3461.643	0.62	1''46	2.703 $\pm$ 0.029	3.953 $\pm$ 0.045	4.965 $\pm$ 0.141	5.626 $\pm$ 0.424	-0.025 $\pm$ 0.003	SMARTS
3468.550	0.95	1''28	2.766 $\pm$ 0.024	3.930 $\pm$ 0.035	4.732 $\pm$ 0.087	5.106 $\pm$ 0.200	-0.020 $\pm$ 0.003	SMARTS
3477.514	0.49	1''08	2.676 $\pm$ 0.024	3.846 $\pm$ 0.044	4.604 $\pm$ 0.099	5.900 $\pm$ 0.482	-0.033 $\pm$ 0.003	SMARTS
3490.481	0.77	1''06	2.670 $\pm$ 0.019	3.825 $\pm$ 0.030	4.689 $\pm$ 0.073	4.799 $\pm$ 0.136	-0.010 $\pm$ 0.003	SMARTS
3502.497	1.13	1''06	2.632 $\pm$ 0.020	3.776 $\pm$ 0.031	4.662 $\pm$ 0.075	4.938 $\pm$ 0.161	-0.013 $\pm$ 0.003	SMARTS
3520.515	0.85	1''34	2.520 $\pm$ 0.025	3.763 $\pm$ 0.038	4.739 $\pm$ 0.112	5.261 $\pm$ 0.306	-0.024 $\pm$ 0.003	SMARTS
3528.450	0.77	1''13	2.587 $\pm$ 0.027	3.743 $\pm$ 0.048	4.901 $\pm$ 0.152	5.322 $\pm$ 0.343	-0.034 $\pm$ 0.003	SMARTS
3676.836	0.50	1''40	2.185 $\pm$ 0.020	3.529 $\pm$ 0.033	4.584 $\pm$ 0.114	5.174 $\pm$ 0.306	-0.030 $\pm$ 0.003	SMARTS
3686.836	0.77	1''22	2.120 $\pm$ 0.015	3.518 $\pm$ 0.025	4.375 $\pm$ 0.066	5.295 $\pm$ 0.258	-0.014 $\pm$ 0.003	SMARTS
3696.825	0.54	1''31	2.101 $\pm$ 0.025	3.614 $\pm$ 0.059	4.354 $\pm$ 0.140	5.088 $\pm$ 0.403	-0.043 $\pm$ 0.003	SMARTS
3704.817	0.76	1''13	2.184 $\pm$ 0.014	3.520 $\pm$ 0.022	4.364 $\pm$ 0.057	4.969 $\pm$ 0.164	-0.006 $\pm$ 0.003	SMARTS
3711.988	1.35	0''99	2.221 $\pm$ 0.007	3.538 $\pm$ 0.008	3.909 $\pm$ 0.011	5.206 $\pm$ 0.046	0.180 $\pm$ 0.003	MDM–RETROCAM
3712.791	1.23	1''03	2.213 $\pm$ 0.013	3.505 $\pm$ 0.020	4.220 $\pm$ 0.044	5.099 $\pm$ 0.162	-0.001 $\pm$ 0.003	SMARTS
3719.804	0.54	1''13	2.173 $\pm$ 0.019	3.586 $\pm$ 0.041	4.506 $\pm$ 0.109	5.092 $\pm$ 0.279	-0.041 $\pm$ 0.003	SMARTS

Note. — HJD is the Heliocentric Julian Day – 2450000 days. The goodness of fit of the image,  $\chi^2/N_{dof}$ , is used to rescale the formal uncertainties when greater than unity (see text). The QSO A–D columns give the magnitudes of the quasar images relative to the comparison stars. The  $\langle \text{Stars} \rangle$  column gives the mean magnitude of the standard stars for that epoch relative to their mean for all epochs.

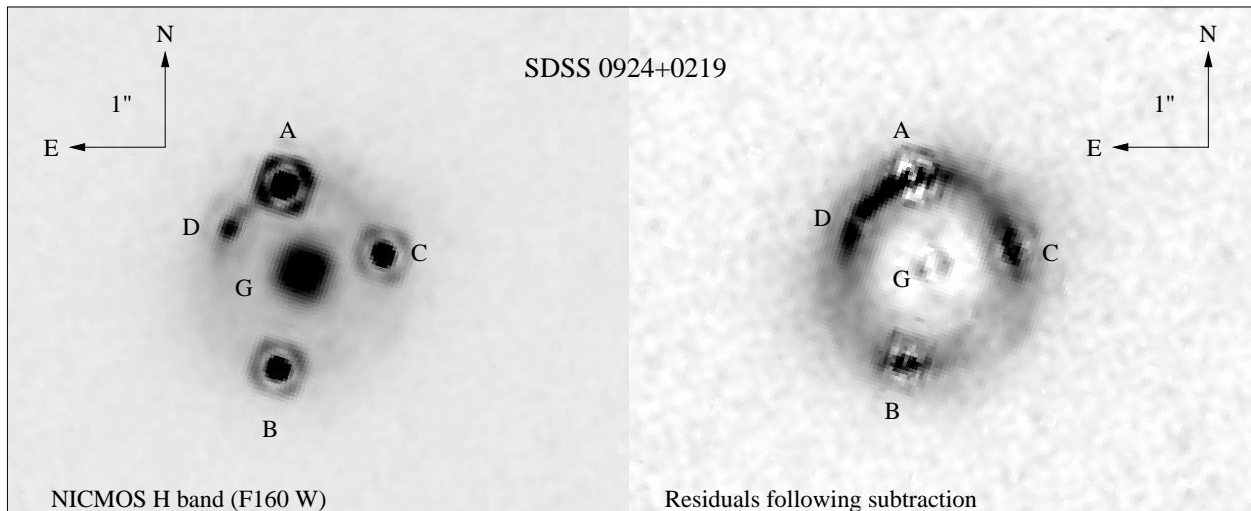


Fig. 1.— *H*-band images of SDSS0924+0219. The left panel shows the original image. Note that image D shows the Airy ring of a point source and is markedly fainter than image A. The right panel shows *H*-band residual near each quasar image after subtracting the four quasar images and the lens galaxy to make the Einstein ring image of the quasar host galaxy more visible. The noisy residuals near each image are largely due to small errors in the PSF models.

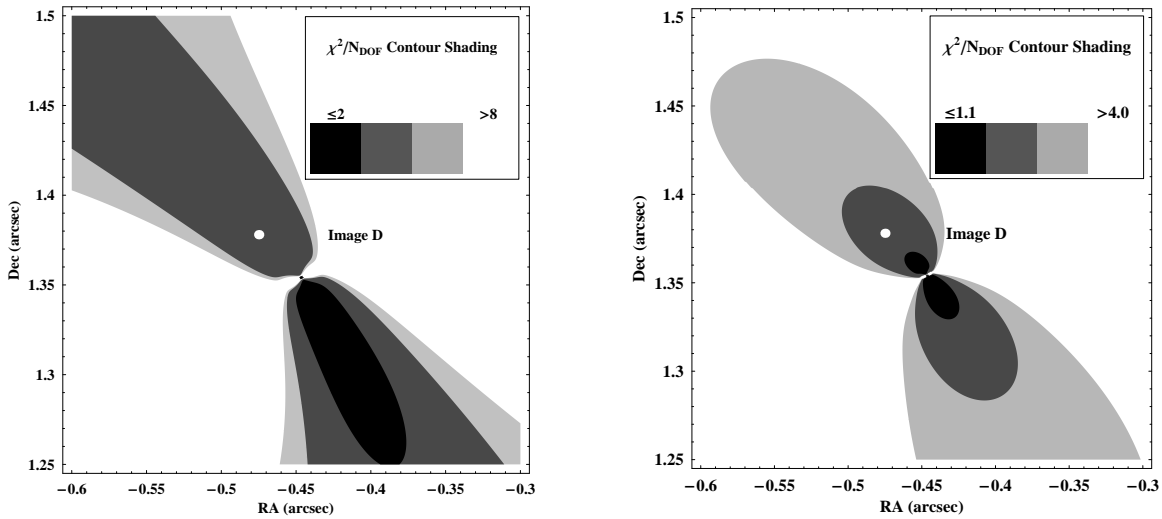


Fig. 2.— Substructure models for the SDSS0924+0219 flux ratio anomaly. The left (right) panels show the regions where a pseudo-Jaffe model with an Einstein radius of  $0''.01$  ( $0''.003$ ) can remove the A/D flux ratio anomaly without significantly worsening the constraints on the quasar image positions or the Einstein ring. The main lens is modeled as a singular isothermal ellipsoid (SIE) and the pseudo-Jaffe models are tidally truncated at  $0''.1$  ( $0''.06$ ). The position of image D is indicated with a white point.  $\chi^2$  contours are indicated in the figure legends.

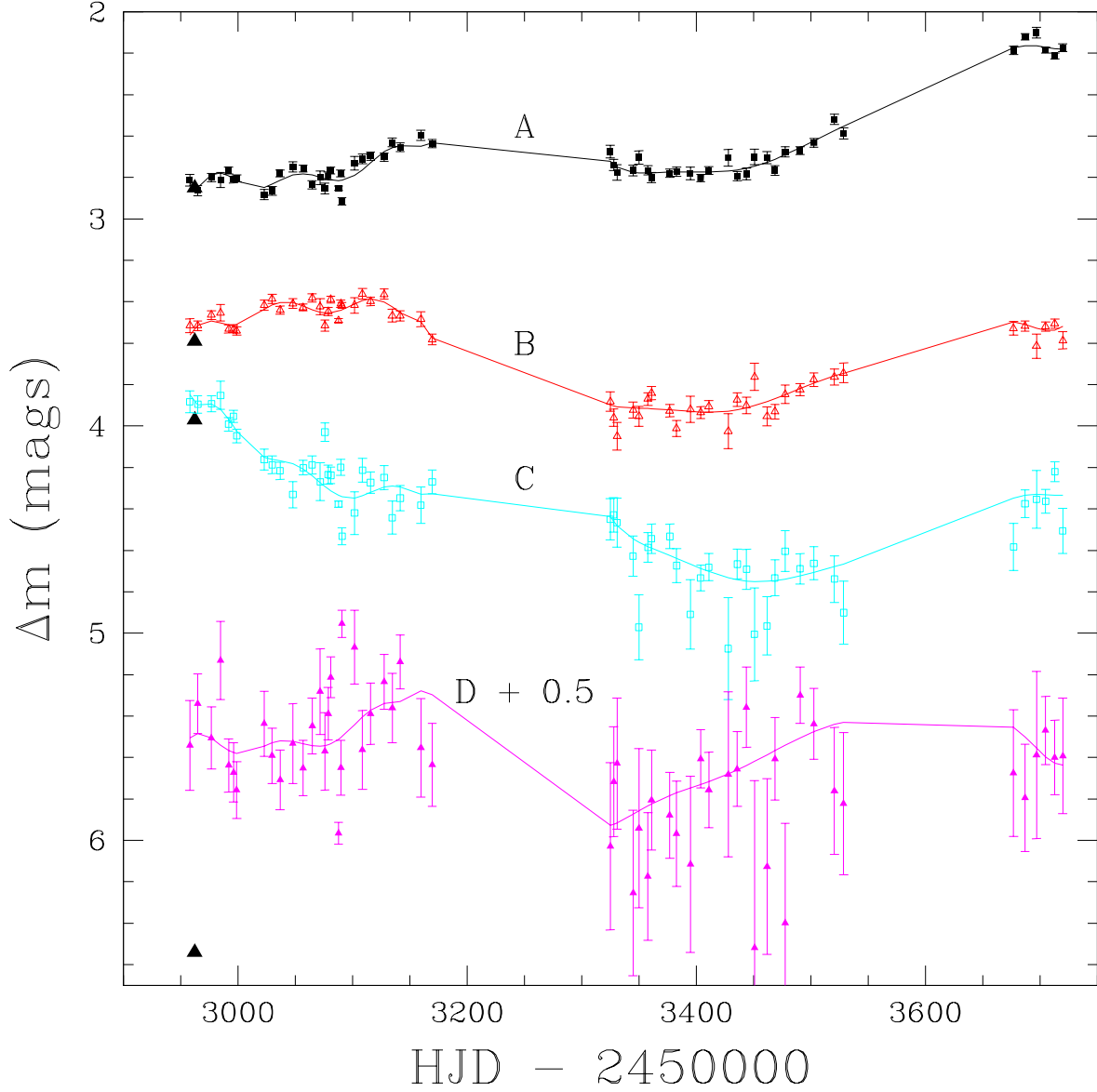


Fig. 3.— SDSS0924+0219 *R*-band light curves for images A–D. The data points for image D are offset to improve their visibility. The curves are derived from a joint, high-order polynomial fit for the source light curve combined with lower order polynomials for the microlensing variability of each image (see Kochanek 2005 for details). Symbols: Image A—solid squares, Image B—open triangles, Image C—open squares and Image D—solid triangles. The large solid triangles at 2962 days are the HST *V*-band photometry referenced to Image A.

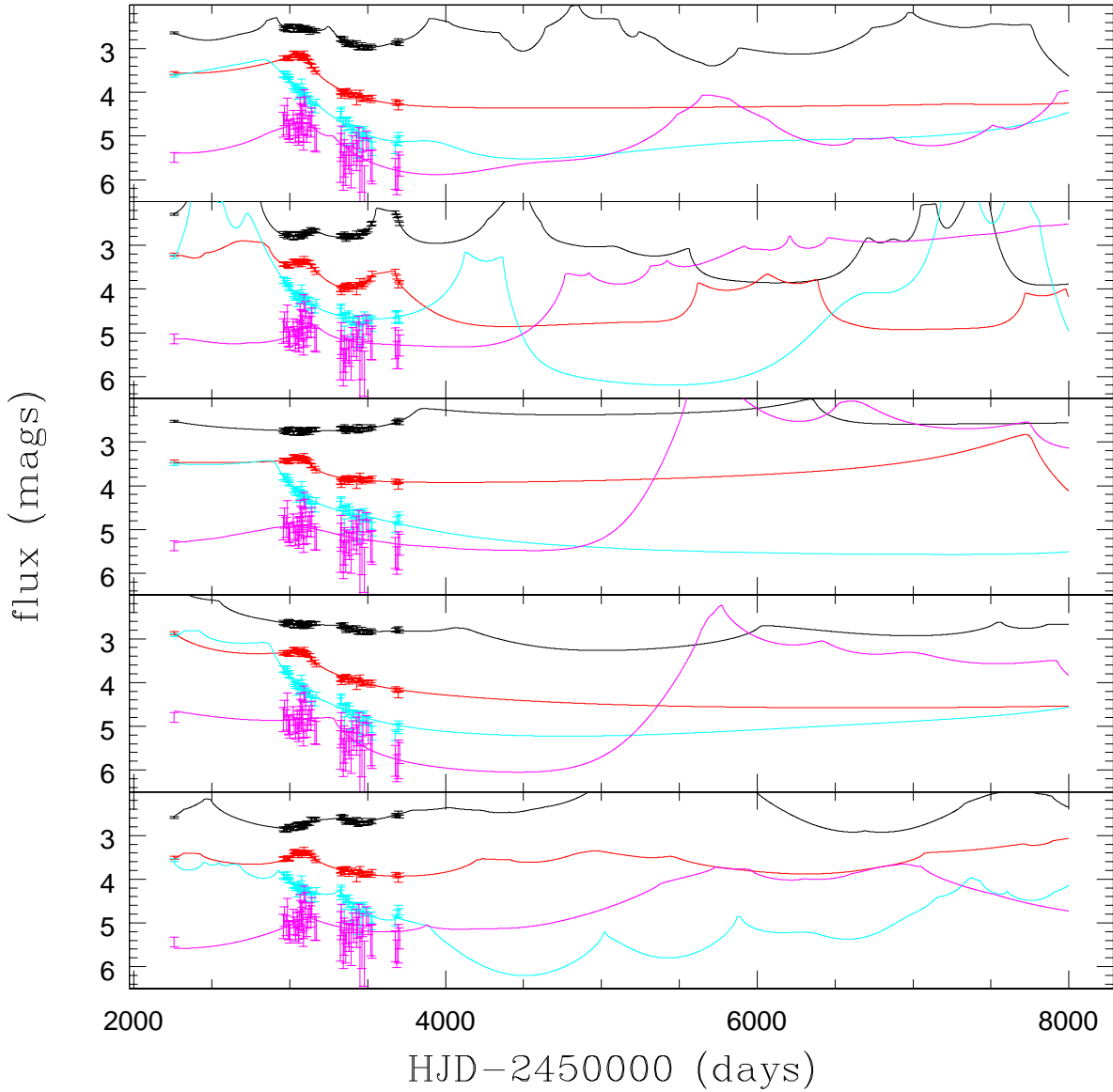


Fig. 4.— The five best fitting  $R$ -band light curves extrapolated for an additional 10 years across their magnification patterns. In order to show the “goodness of fit” of the theoretical microlensing lightcurves, we plot as points the observed image flux minus our model for the intrinsic variability of the source. In most of these light curves we see a brightening of images D and C.

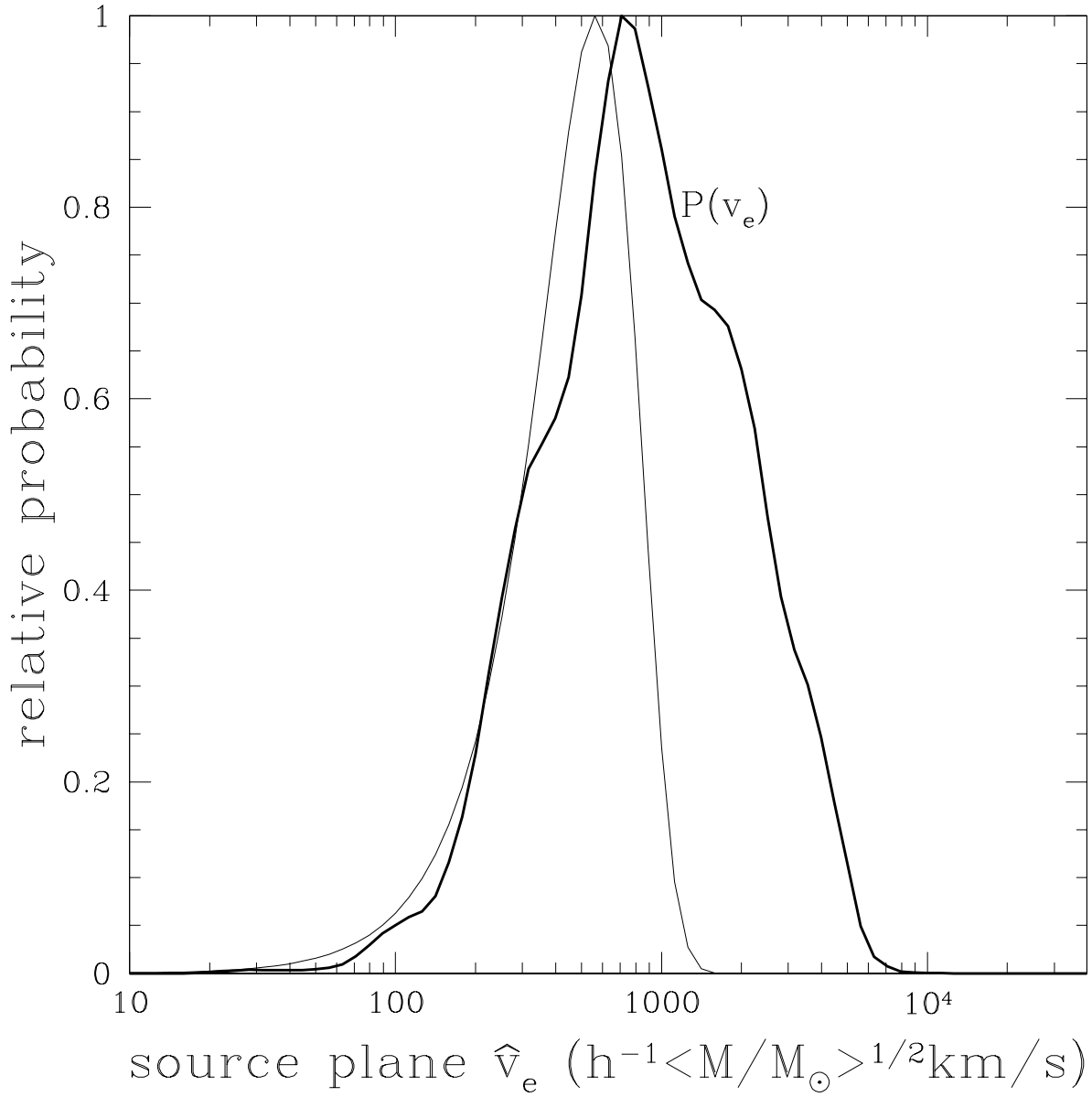


Fig. 5.— Normalized probability distribution for the effective source plane velocity ( $\hat{v}_e$ , heavy solid line) as compared to our estimated probability distribution for the true source plane effective velocity  $v_e$  (light solid line). Since the average microlens mass  $\langle M \rangle$  is related to the two velocities by  $\hat{v}_e \propto v_e/\langle M \rangle^{1/2}$ , high (low) ratios of  $\hat{v}_e/v_e$  correspond to low (high) mass microlenses.

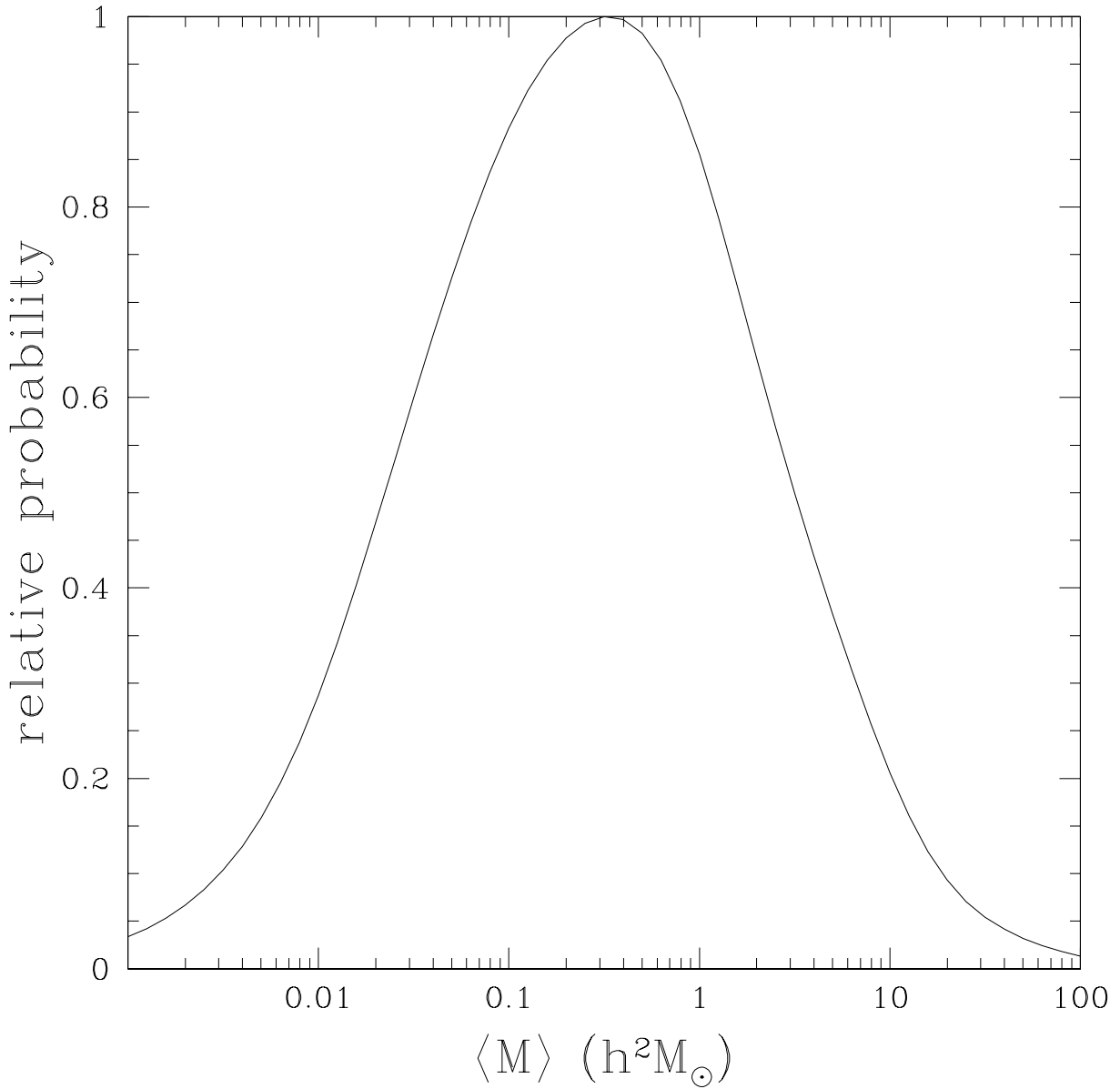


Fig. 6.— Probability distribution for the average stellar mass  $\langle M \rangle$  in the lens galaxy. The uncertainty is relatively large because  $\langle M \rangle \propto v_e^{-2}$ , but it is consistent with normal stellar populations.

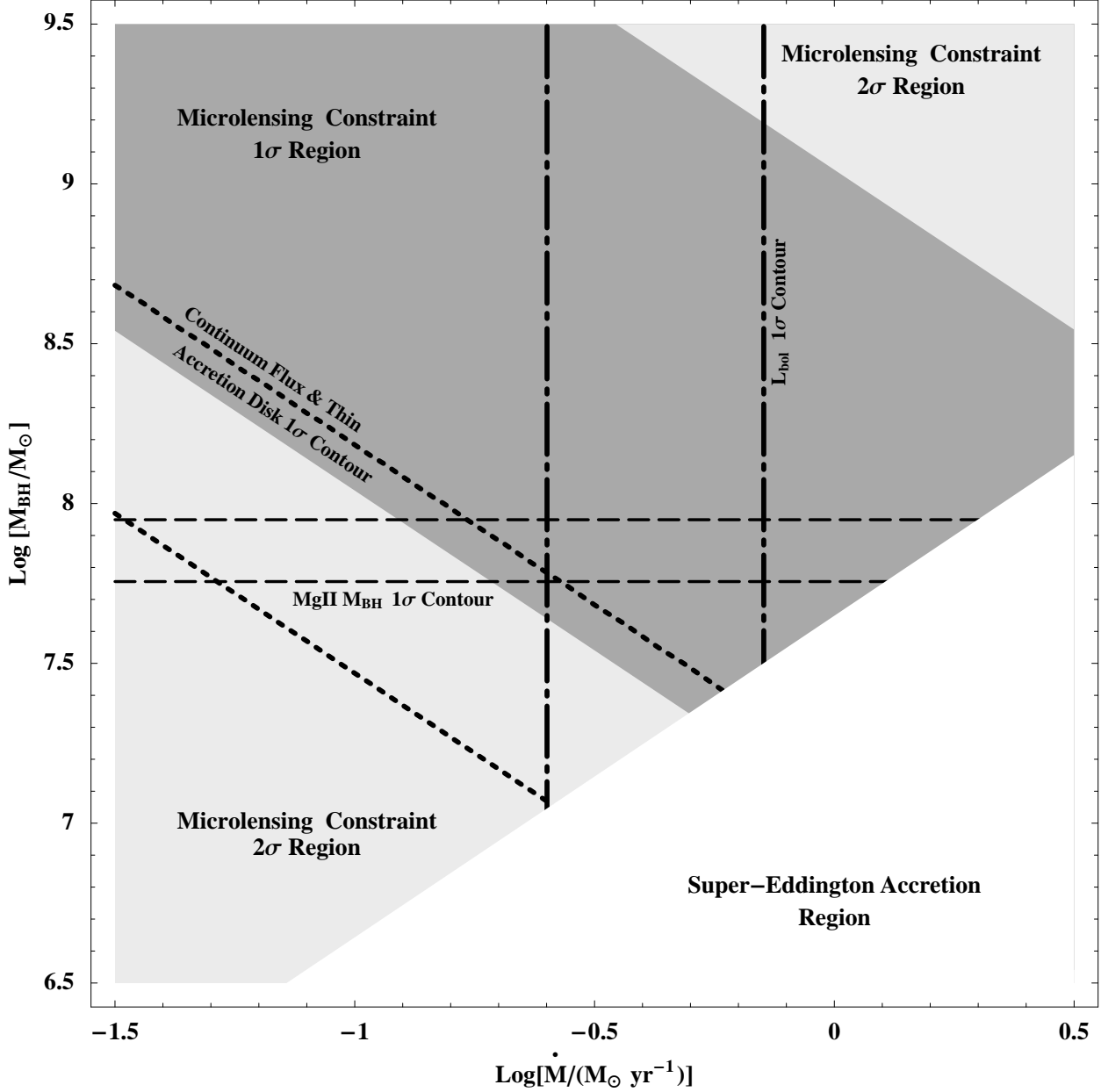


Fig. 7.— Constraints on the mass and accretion rate of the SDSS0924+0219 quasar. The dashed horizontal lines show the estimated black hole mass based on the Mg II 2800Å emission line width. The vertical dash-dotted lines show the estimated accretion rate assuming a radiative efficiency of 10% and the Kaspi et al. (2000) method for estimating the bolometric luminosity. The dotted lines show the constraint on the product  $M_{BH}\dot{M}$  from the continuum flux and thin accretion disk theory. The shaded regions show the constraint on the product  $M_{BH}\dot{M}$  from the microlensing data with a prior of  $0.1 M_{\odot} < \langle M \rangle < 1.0 M_{\odot}$  on the mean mass of the microlenses. The accretion is super-Eddington in the lower right corner, so we terminated the constraints on the line where  $L = L_{Edd}$ . All values plotted are scaled to  $h = 0.7$ .

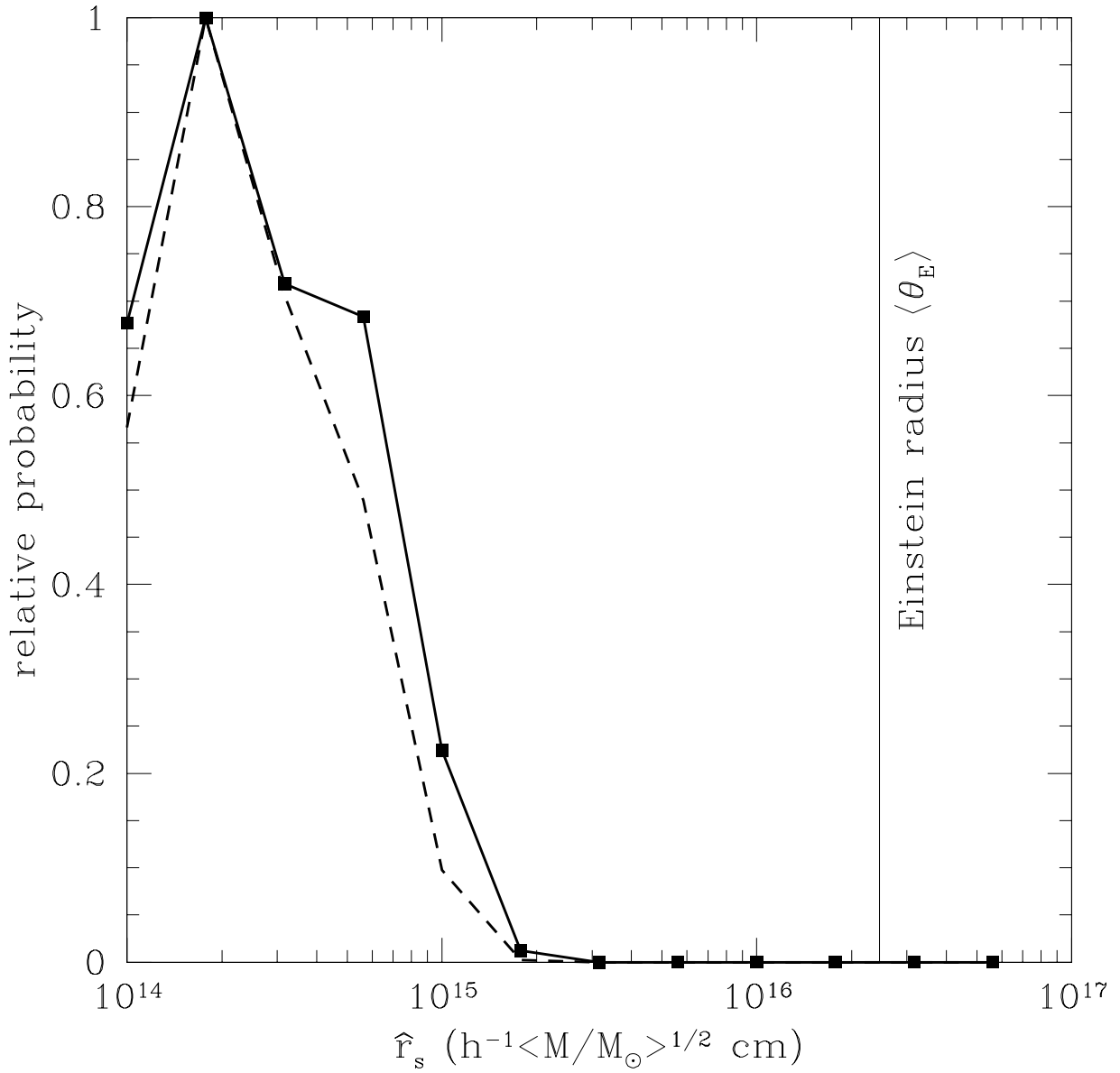


Fig. 8.— Probability distributions for the scaled source size  $\hat{r}_s$ . The heavy dashed line shows the estimate for  $\hat{r}_s$  including a prior of  $0.1 M_\odot < \langle M \rangle < 1.0 M_\odot$  on the mass of the stars. The vertical line shows the Einstein Radius  $\langle \theta_E \rangle$  of the average mass star.

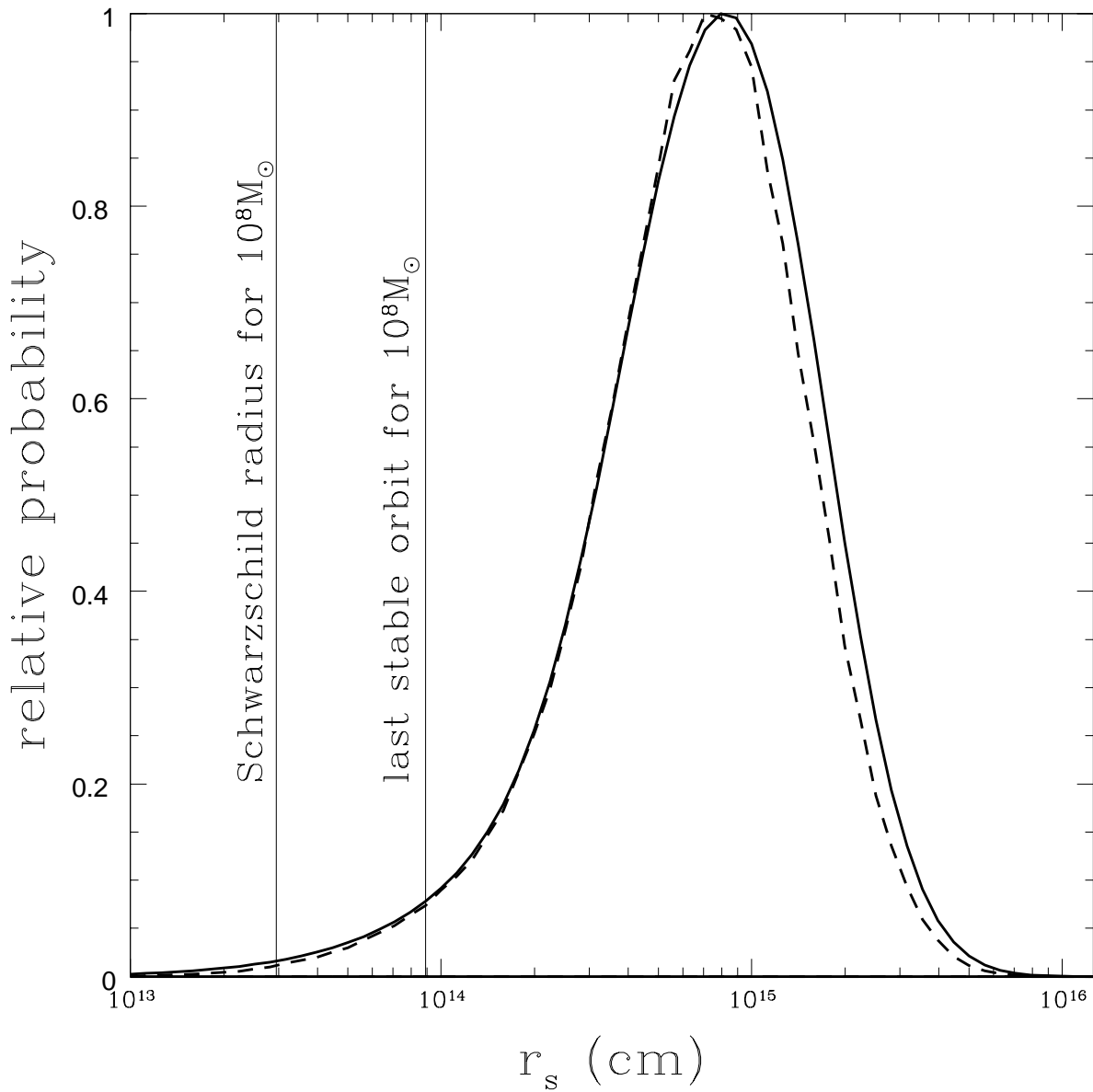


Fig. 9.— Probability distributions for the physical source size  $r_s$ . The dashed curve shows the estimate for  $r_s$  with a prior of  $0.1 M_\odot < \langle M \rangle < 1.0 M_\odot$  on the mean mass of the microlenses. The vertical line shows the Schwarzschild radius  $R_{BH} = 2GM_{BH}/c^2$  of a  $10^8 M_\odot$  black hole. The last stable orbit for a Schwarzschild black hole is at  $3R_{BH}$ .

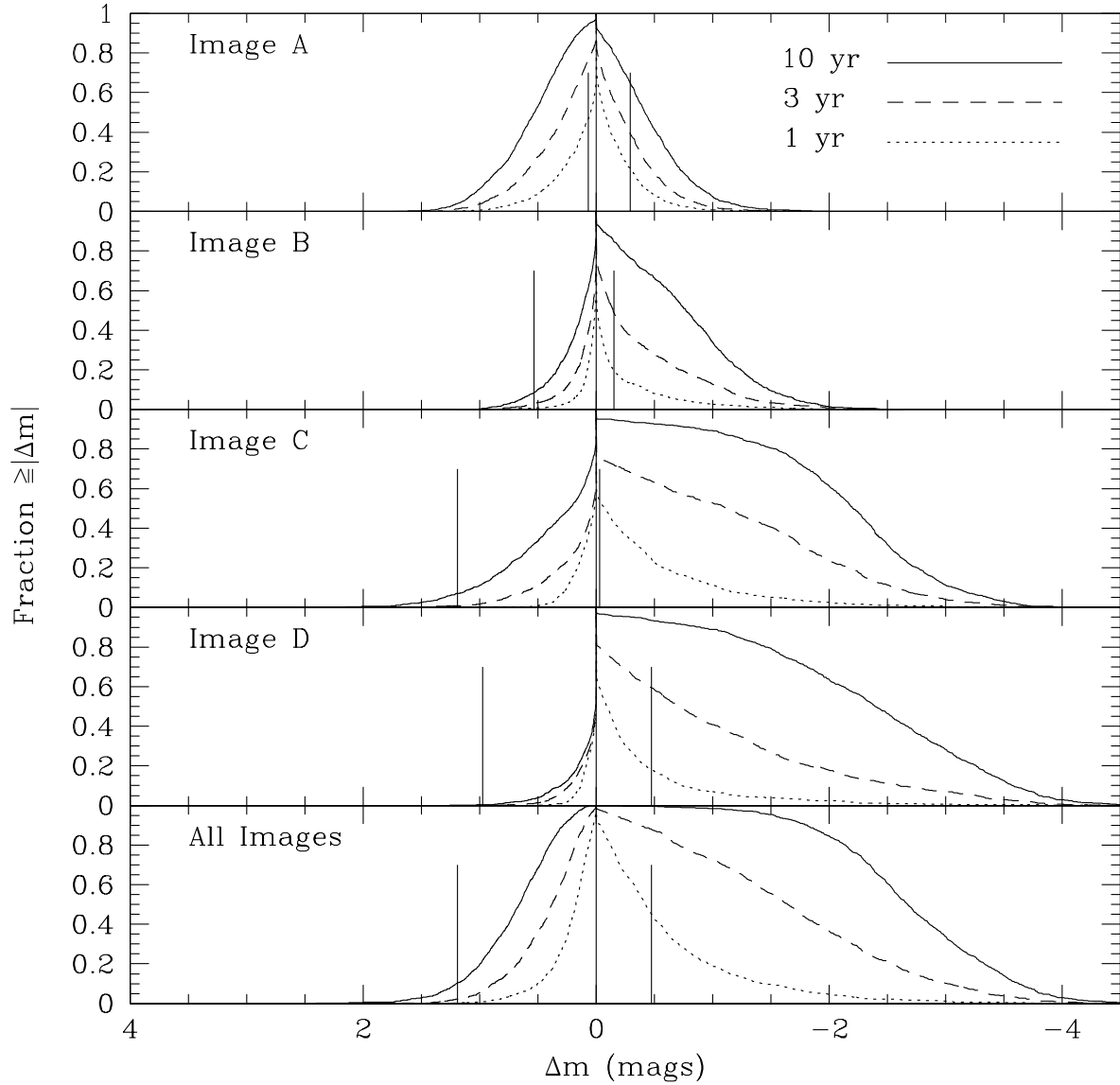


Fig. 10.— Fraction of light curves with  $\chi^2/N_{DOF} < 2.3$  that undergo a change in magnification larger than  $\Delta m$  magnitudes towards either brighter (right) or fainter (left) fluxes after one (dotted), three (dashed) or ten (solid) years. The vertical lines show the largest observed  $\Delta m$  for our present light curves.